Elastic bound modes in the continuum in architected beams

Adib Rahman and Raj Kumar Pal

Phys. Rev. Applied **21**, 024002 — Published 1 February 2024

DOI: 10.1103/PhysRevApplied.21.024002

Observation of elastic bound modes in the continuum in architected beams

Adib Rahman and Raj Kumar Pal*
Department of Mechanical and Nuclear Engineering,
Kansas State University,
Manhattan, Kansas 66506, USA

(Dated: December 11, 2023)

We report the experimental observation of an elastic bound mode in the continuum (BIC) in a compact region of an architected beam. We consider a long slender beam with rigid masses attached at periodic intervals, with a compact segment bounded by four protruding side beams. The key idea is to seek a mode where the side beams move out-of-phase with the compact region, thereby nullifying the forces and moments outside this region and resulting in a bound mode. The structure is modeled using Euler-Bernoulli beam theory and the side beams are designed by imposing equilibrium constraints required for a BIC. Multiple BICs are found in the compact region, and for each BIC, we find a one-parameter family of BIC supporting side beam designs. The predictions are verified by three-dimensional finite element simulations, followed by their experimental observation using laser Doppler vibrometry in a macro-scale structure. Our approach allows to achieve BICs in an arbitrary sized compact region of the architected beam. Our findings may open avenues for confining elastic wave energy in compact regions for applications in sensors and resonators.

I. INTRODUCTION

Bound modes in the continuum (BICs) are a unique class of localized modes with two key properties: their wave amplitude diminishes to zero outside a compact region and their frequency is in the continuous spectrum (pass band) of bulk propagating modes [1]. In contrast, conventional bound modes reside within bandgaps, and the localized modes encountered in the passband typically exhibit leakage, with the wave amplitude gradually decreasing from the center of the wave [2–4]. The concept of BICs originated in quantum mechanics, introduced by von Neumann and Wigner in 1929, who utilized a complex artificial potential [5]. It was regarded as a mathematical anomaly, as such complex potentials were not possible in real materials. BICs were subsequently predicted and observed in several classical wave systems [6, 7]. Notably, in 1966, BICs were experimentally observed in acoustics through the 'wake shedding experiment' [8]. Today, BICs have become an active area of research across various scientific disciplines due to their leak free energy storing capacity with very high quality factor (Q factor) [9]. Potential applications of BICs encompass lasing [10–12], sensing [13], filtering [14, 15], supersonic surface acoustic device [16, 17], vibration absorption [18], and wave guiding [19–21].

Recent advancements in manufacturing techniques have opened up new possibilities for exploring BICs in complex structures, particularly in the domains of photonic metamaterials. Two major types of BICs are symmetry-protected and accidental. Symmetry-protected BICs arise from the mismatch between the spatial symmetry of a localized mode and the symmetry of the propagating modes. Experimental observations of such symmetry-protected BICs have been reported in various systems, such as dielectric slabs with square arrays of cylinders [22], periodic chains of dielectric disks [23], and optical waveguides [24]. On the other hand, accidental BICs can be achieved through precise system parameter tuning to cancel their coupling with bulk propagating waves. Examples of this category is the Fabry-Perot BIC [25, 26], where the BIC is formed through the destructive interference of waves. In addition to these two types of BICs, recent research has explored quasi-BICs (QBICs) which have high Q factors [27, 28]. As true BIC-supporting structures are limited, quasi-BICs are emerging as an alternative.

In contrast to photonics, a major challenge in achieving elastic BICs is the simultaneous presence of transverse and longitudinal waves with distinct dispersion relations. BICs should not couple or hybridize with any propagating modes present in an elastic body. Haq and Shabanov first theoretically predicted Fabry-Pérot BICs for in-plane wave with scatterers [29], using distinct densities but same Lamé constants for the background material and scatterers. Cao *et.al.* [18, 30] experimentally demonstrated wave confinement at the boundary of an elastic plate for transverse waves incident at a specific angle. Their design uses an array of resonators embedded at the plate boundary. Fan *et.al* [31] observed BIC in a non-Hermitian system by exploiting damping and boundary conditions. BICs have also been observed in multi-physics domains, including in chip scale ring-shaped optomechanical microresonators [32], slab-on-substrate phononic crystals [33], elastic bar with air-encapsulated cavity [34]. All these BICs require specific material properties, boundary conditions, geometric features or properties like damping and multi-physics interactions. For practical applications, it is desirable to have a general framework that can translate across material properties and generate BICs in arbitrary sized compact

* rkpal@ksu.edu

regions.

This work builds on our prior work [21], where we predicted how a family of BICs can be achieved in an arbitrary compact region of a spring-mass system by exploiting symmetry constraints. Here, we extend this concept to realize BICs in a compact region of an architected beam. In contrast to spring-mass chains, beams are continuous structures with multiple degrees of freedom at each point, namely transverse displacements and rotations. These degrees of freedom impose additional conditions for BICs. Here, we consider a periodic architected beam having an array of rigid masses. To achieve BICs in a compact region, four side beams are added, and the key idea is that they move out-of-phase with the periodic beam to nullify forces and moments at their joints. Compared to previous works, our concept provides a framework to confine an elastic wave at an arbitrary location in a beam structure. The frequency and length of confined region can be independently varied using the size and location of the rigid masses. In addition, the concept translates across material properties and length scales.

The outline of the paper is as follows: section II presents the design and modeling approach. The structure is modeled using $1D$ Euler-Bernoulli beam theory. Section III presents the BIC mode shapes determined using $1D$ finite element analysis and reports a 1-parameter family of BIC supporting side beam designs. In section IV, $3D$ finite element simulations and laser Doppler vibrometry based experimental measurements are presented, that verify and validate the existence of a BIC in the architected structure. The simulations are done using the beam theory-based design as a starting point to finalize a structure that simplifies fabrication. Finally, the conclusions, along with various sources of error and possible future extensions are presented in section V.

II. PROPOSED CONCEPT AND MODELING APPROACH TO DESIGN COMPACT REGION

We first introduce the proposed architected beam and discuss the key idea of achieving BICs in a compact region by adding side beams. These side beams are designed by modeling the structure using a one-dimensional ($1D$) Euler Bernoulli beam theory. A description of this modeling approach is presented, followed by its numerical discretization procedure.

A. Architected beams with side segments and symmetry consideration

Let us consider a homogeneous beam with rigid masses attached at periodic intervals of distance l. An example is shown in the central beam in Fig. 1(a). We call this periodic architected beam as the main beam. Figure 1(b) displays a unit cell of the main beam with the key geometric variables labeled. It is a slender beam with rectangular cross-section and has two identical rigid cylinders at its center, one each at the top and bottom. Note that rigid masses in the main beam allows independent control over the length of region in which a BIC mode is confined and its frequency.

Our objective is to achieve a BIC in an arbitrary compact region, for example between the cross-sections labeled A and B in Fig. 1(a). We will model this architected structure using one-dimensional ($1D$) beam theory, which assumes that the beam deforms such that each cross-section remains rigid. Under this assumption, the degrees of freedom are the 3 translations and 3 rotations of each cross-section along the beam's axis. We restrict attention to long wavelengths, compared to the beam thickness and low frequencies, i.e., in the first pass band of the beam. The lower frequency band has flexural modes with displacement along z. For such modes, it suffices to consider two degrees of freedom at each cross section: transverse displacement u along z and rotation θ about y-axis, with the latter accounting for bending. The presence of side beams couples the torsional (rotation about x) and flexural modes near the compact region. However, as we discuss below, for BIC modes, the rotation about x is cancelled due to symmetry and thus, the number of relevant degrees of freedom at each point along the beam cross-section is two.

A BIC between sections A and B will be a mode confined in this region and with zero displacement and rotation at all points outside, i.e., in the segments AP and BQ. Our approach is to add side beams, as displayed in Fig. 1(a), that cancel the motion outside the compact region. Let us first present the conditions that ensure a bound mode in the compact region. We enforce zero displacement, rotation, net force and moment at the boundaries of the compact region, i.e., at sections A and B. These conditions at section A may be written as

$$\sum F_{zA} = 0,\ \sum M_{xA} = \sum M_{yA} = 0,\ u_A = 0,\ \theta_A = 0. \tag{1}$$

Note that only the contributions from the compact region and the side beams are considered in the forces and moments in Eqn. (1).

To see why the above conditions imply that segment AP in Fig. 1(a) is at rest, we consider an initial boundary value problem on the segment AP when Eqn. (1) is satisfied. This segment has no external forces and its boundaries have zero displacement. The zero displacement field ($\boldsymbol{u} = [u_x\ u_y\ u_z]^T = \mathbf{0}$) throughout the segment AP is a valid solution since it satisfies the equilibrium conditions at each point as well as all the boundary conditions. Since the governing equations, namely the Cauchy equations for elastodynamics, or the one-dimensional Euler-Bernoulli beam theory, are linear, the solution ($\boldsymbol{u} = \mathbf{0}$) is unique. Thus the conditions in Eqn. (1) ensure zero displacement in the segment AP, regardless of its size or the boundary type at P. Similar conditions to Eqn. (1) at section B ensure that the segment BQ is at rest, thereby implying a BIC confined in the segment AB, along with

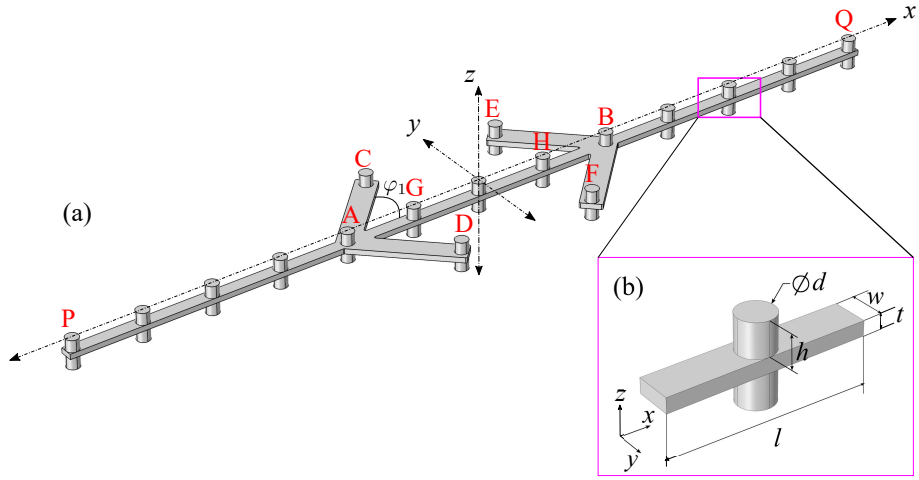

FIG. 1. (a) Schematic of proposed architected beam: rigid masses attached at periodic intervals along a homogeneous beam. Four side beams are added to get a BIC between A and B. (b) A unit cell of the periodic beam with the key geometric variables labeled.

their side beams.

Let us discuss how the side beams in Fig. 1(a) induce BICs. The key idea is to have a mode where the side beams move out of phase, i.e., in opposite direction to the main beam, thereby cancelling the net force and moment at sections A and B. In addition, as we explained above, enforcing zero displacement and rotations at these sections results in the far field being at rest. Finally, let us remark on the reason for having two side beams, one on either side, at sections A and B. A single side beam will induce torsional rotation about the main beam axis due to the moment component M_x. To cancel this moment, a second side beam is added. The two side beams on either side at A thus move in-phase with each other, but out-of-phase with the main beam. We will show later in Sec. III a family of side beams that can satisfy Eqn. (1), i.e., cancel displacement, rotation, force and moment at A and B.

We choose all the side beams to be identical and arrange them so that the center of the compact region between sections A and B has reflection symmetry about both x and y axes. Note that BICs do not require these symmetries and they are chosen to simplify the side beam design. Indeed, the only requirement to ensure zero displacement and rotation outside the compact region is to satisfy the conditions of Eqn. (1) at sections A and B. We remark here that the full design space of distinct side beams is sufficiently large, with multi-parameter families of solutions that satisfy these conditions. Imposing the constraints arising for symmetry, the problem of inducing BICs reduces to determining suitable side beams. As we are considering that the side beams' arrangement is reflection symmetric about the x and y axis, determining one side beam's design will suffice to complete the beam structure that can support BIC at a particular frequency.

Let us discuss how these reflection symmetries and equilibrium conditions impose restrictions on resulting bound mode shapes in the compact region. Each symmetry can be represented by a linear transformation operator. This operator maps the position vectors of each point in the structure to its corresponding reflected point. In addition, the mode shapes are eigenvectors of this operator [35]. The reflection symmetry operator has two eigenvalues: $\lambda = \pm 1$ and the bound mode shapes are thus even ($\lambda = 1$) or odd ($\lambda = -1$) in the compact region about the symmetry axis. Let us analyze the consequence of reflection symmetry about x axis. An odd mode shape about the x axis will induce a moment and thus rotation about x at sections A and B as the side arms move in opposite directions. The sections to the left of A and right of B will thus not be at rest and a bound mode is thus not possible with an odd mode shape about the x axis. In summary, a bound mode shapes in the compact region will be either even or odd about the y axis and even about the x axis.

B. Modeling with Euler-Bernoulli beam theory and numerical procedure

Let us derive the governing equations for free vibrations of the structure based on $1D$ beam theory and discuss the finite element based procedure to solve them. Let $u(x,t)$ and $u_p(x,t)$ denote the transverse displacements of the main beam and side beam p, respectively. The action functional for this structure is given by

$$S = \int_0^T \int_0^L \left[\frac{\rho A \dot{u}^2}{2} - \frac{EI\left(u''\right)^2}{2} + \sum_{p=1}^{N} \left(\frac{m\dot{u}^2}{2} + \frac{I_r \dot{\theta}^2}{2} \right) \delta(x - pl) \right] dxdt$$
$$+ \sum_{p=1}^{4} \frac{1}{\cos\varphi_p} \int_0^T \int_0^{L_p} \left[\frac{\rho A \dot{u}_p^2}{2} - \frac{\cos^4\varphi_p EI\left(u_p''\right)^2}{2} + \left(\frac{m_p \dot{u}_p^2}{2} + \frac{\cos^2\varphi_p I_{rp} \dot{\theta}_p^2}{2} \right) \delta(x - L_p) \right] dxdt \quad (2)$$

Here u' and $\dot{u}$ denote partial derivatives of u with respect to x and t, respectively, $\theta = u'$ is the rotation of the section and $L_p/\cos\varphi_p$ is the length of side beam p. E, I, ρ and A are the Young's modulus, bending moment of inertia, density and cross-section area, respectively. The attached cylinders are assumed to be rigid with diameter d. The bending moment of inertia is $I = wt^3/12$ for a beam with width w and thickness t. φ_p is angle of side beam p with respect to the x-axis. We seek harmonic solutions at frequency ω and impose a displacement field of the form $u(x,t) = u(x)e^{i\omega t}$ to replace the time derivatives by $i\omega$. The displacement field satisfies the Euler Lagrange equations, obtained by setting variation of S to zero. This condition gives

$$\delta S = \int_0^L \left[-\omega^2 \left(\rho A u \delta u + \sum_{p=1}^{N} (m u \delta u + I_r u' \delta u') \delta(x - pl) \right) - EI u'' \delta u'' \right] dx$$
$$+ \sum_{p=1}^{4} \frac{1}{\cos\varphi_p} \int_0^{L_p} \left[-\omega^2 \left(\rho A u_p \delta u_p + \left(m_p u_p \delta u_p + \cos^2\varphi_p I_{rp} u_p' \delta u_p' \right) \delta(x - L_p) \right) - \cos^4\varphi_p EI u_p'' \delta u_p'' \right] dx = 0. \quad (3)$$

Now, let us discuss the numerical procedure to discretize and solve the above equation. We use a finite element approximation, where unknown degrees of freedom are restricted to be the displacements u and rotations u' at the locations of attached masses. We express u and u' at a point in the structure as a weighted sum of piecewise cubic polynomials, i.e., having continuous first derivatives, and the weights being the degrees of freedom. We seek a solution that satisfies the governing equation (3) for any perturbation fields δu and $\delta u'$ that lies in the same space spanned by the degrees of freedom. Explicit expressions for the polynomials and the resulting equations are presented in the appendix. The resulting discretized eigenvalue problem for the structure may be written in the matrix form as

$$\omega^2 \boldsymbol{M}\boldsymbol{u} = \boldsymbol{K}\boldsymbol{u}. \quad (4)$$

Here $\boldsymbol{u}$ is the vector of unknown degrees of freedom, i.e., displacements and rotations at masses, and $\boldsymbol{M}$, $\boldsymbol{K}$ are the discretized mass and stiffness matrices, respectively.

III. NUMERICAL SOLUTION OF ARCHITECTED BEAMS SUPPORTING BICS

In this section, the mode shapes of BICs and a family of side beams that support these BICs are determined for a given main beam. Although our studies are presented for a specific choice of compact region, the concept and approach can be extended to an arbitrary sized compact region and material properties. A two step process is used to design BIC supporting structures using the beam model introduced above in Sec. II B. The first step is to determine the bound mode frequencies by imposing zero displacement and rotation at sections A and B in the main beam. The next step is to determine the side beam dimensions that satisfy the equilibrium conditions required to keep sections A and B at rest. Finally, we verify if these modes are indeed BICs, i.e., if their frequency lie in a pass band. This is done by performing a dispersion analysis that yields the pass and stop band frequencies.

A. Bound mode frequencies and design of side beams

Having derived the governing equations for the proposed structure, let us now solve them numerically to determine BICs. The first step is to determine the bound modes by considering the compact region of the main beam only and explicitly enforcing zero displacement and rotation at sections A and B in Fig. 1(a). The resulting modes will, in general, not satisfy equilibrium conditions at sections A and B. The second step is to determine the

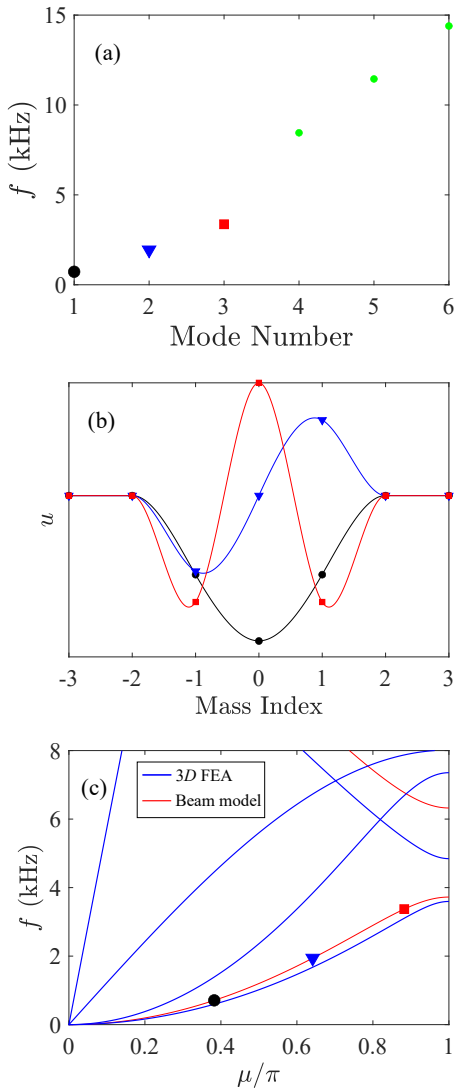

FIG. 2. (a) Frequencies of bound modes in the compact region of Fig. 1(a). (b) Mode shapes of first 3 modes, u is transverse displacement along the main beam. Markers indicate rigid mass locations, with similar marker in (a) for their frequency. (c) Dispersion diagram of the main beam from $1D$ beam theory and $3D$ elasticity. The first three mode frequencies lie on the lowest flexural band and are thus BICs.

side beam dimensions so that the total structure (main and side beams together) satisfy the equilibrium conditions at sections A and B. In these mode shapes, sections A and B will thus be at rest and have zero net force and moment, thereby ensuring that parts outside the compact region will be at rest. Thus, this procedure ensures bound modes in the structure.

In the first step, to determine the natural frequency and mode shape of BICs, we use material properties of Aluminum 6061 with Young's modulus (E = 68.9 GPa, Poisson's ratio $\nu = 0.3$ and density ρ = 2700 kg/m^3) for the beam and Neodymium Magnet N35 (cylinder density, ρ_c = 7537.6 kg/m^3) for the cylinders considering ease of fabrication. The key geometric variables (l, w, t, d, h) in the unit cell, see Fig. 1(b) are chosen to be (27.5 mm, 5 mm, 2.032mm, 5mm, 4.6mm). The bound mode shapes and frequencies are determined by solving the eigenvalue problem (4) in the compact region with zero displacement and rotation boundary conditions. Figure 2(a) displays the six bound mode frequencies.

Next, we need to determine the side beam dimensions so that the structure supports BIC in the compact region. There are several geometric variables for the side beams as shown in Fig. 1(b) for a unit cell as well as the angle between the main the beam and side beam AC, φ_1 as shown in Fig. 1(a). Different sets of the geometric variables for side beams can give BICs in the compact region. We fix φ as 45° to simplify the problem. Also, for ease of fabrication, the beam thickness and the cylinder diameters in the side beams are chosen to be the same as that in the main beam. Thus the design reduces to determining three geometric variables: length (l_s), width (w_s) of the side beams, and the cylinder height (h_C) at section C in Fig. 1(a).

Let us summarize the conditions on a side beam displacement field u_p needed to get a BIC. These conditions ensure that section A and the region to the left of it will be at rest. Recall the key idea that the two identical side beams at section A, as in Fig. 1(a) move out of phase with the main beam, thereby canceling the force and moment at A. Its displacement field has to satisfy the governing equations (3) at the bound mode frequency ω under fixed boundary conditions at A ($u_p = 0$ and $u_p' = 0$). In addition, the resulting forces and moments from the side and main beams should add to zero so that section A is in equilibrium. Under the considered $1D$ beam theory, the force and moment at section A are given by

$$F = EIu''' + \sum_{p=1}^{2} \cos^3\varphi_p \, u_p''',$$

$$M = EIu'' + \sum_{p=1}^{2} \cos^2\varphi_p \, EI_p u_p''.$$

Now, we derive the discrete approximations of the above conditions for the side beam having section C in Fig. 1(a). A side beam is modeled using a single finite element and the degrees of freedom are the displacements and rotations at the two ends (A and C). Since we seek solutions with section A fixed, the displacement field simplifies to $u_p(x) = N_3(x/l_s)\theta_C + N_4(x/l_s)u_C$. Explicit expressions for N_3, N_4 are presented in appendix. Under this approximation, the governing equations of side beams and the equilibrium conditions at A then reduce to

$$\delta\theta_C = 0 \implies \left(\frac{4EI_s}{l_s} - \frac{\omega^2 m_s}{420}(4l_s^2 + I_C)\right)\theta_C + \left(\frac{11\omega^2 m_s}{210} l_s - \frac{6EI_s}{l_s^2}\right) u_C = 0, \quad (5a)$$

$$\delta u_C = 0 \implies \left(\frac{11\omega^2 m_s}{210} l_s - \frac{6EI_s}{l_s^2}\right)\theta_C + \left(\frac{12EI}{l_s^3} - \frac{\omega^2 m_s}{420}(156 + m_C)\right) u_C = 0, \quad (5b)$$

$$F_A = 0 \implies \frac{4EI_s}{l_s}\theta_C - \frac{12EI_s}{l_s^2} u_C - \frac{2EI}{l_e}\theta_G + \frac{6EI}{l_e^2} u_G = 0, \quad (5c)$$

$$M_A = 0 \implies \frac{12EI_s}{l_s^2}\theta_C - \frac{24EI_s}{l_s^3} u_C - \frac{6EI}{l_e^2}\theta_G + \frac{12EI}{l_e^3} u_G = 0. \quad (5d)$$

Here $m_s = \rho l_s w_s t$ and $I_s = w_s t^3/12$ are mass and bending moment of inertia of the side beam, respectively, while $m_C = \pi \rho_c d^2 h_C/4$ and $I_C = m_C/12(3d^2/4 + h_C^2)$ are mass and mass moment of inertia of the cylindrical mass at section C. u_G and θ_G are the displacement and rotation at section G, corresponding to the mode shape of the compact region at frequency ω (see Fig. 2(a,b)). The force and moment balance constraints assume that the two side beams at A move in phase. Indeed, as discussed earlier, a BIC mode shape is symmetric about the x-axis.

The conditions for getting a BIC mode lead to a system of four nonlinear equations (5) with five unknown variables $(u_C, \theta_C, l_s, w_s, h_C)$ related to the side beams. To determine them, l_s is set to different fixed values in a wide range and the remaining variables are determined using the Newton-Raphson method. We determined side beam dimensions that support the lowest frequency bound mode at 713 Hz, denoted by a black marker in Fig. 2(a). Figure 3 displays a 1-parameter family of solutions that we obtained as l_s is varied. Side beams for every solution in Fig. 3 induce the bound mode shown by the black curve in Fig. 2(b). For the chosen main beam, we are unable to find any valid solutions for side beams with rigid masses removed (corresponding to rigid cylinder height $h_C = 0$). Similarly for the frequencies marked by blue triangle and red square, we find families of design parameters which support the corresponding bound modes in Fig. 2(b). These design parameter are displayed in the appendix, Fig. 10.

B. Dispersion analysis of the architected beams

To confirm if the bound modes in Fig. 2(b) are indeed BICs, i.e., if their frequency lies in the pass band, we do a dispersion analysis of the main beam, which is periodic with unit cell in Fig. 1(b). We work with the discrete approximation, where the degrees of freedom are (u_n, θ_n) at a section having rigid mass labeled n. We seek

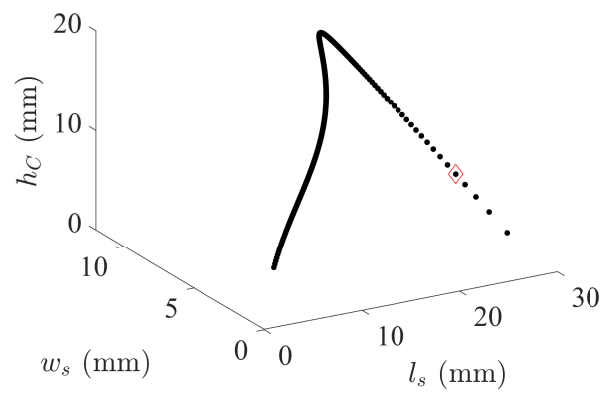

FIG. 3. A 1-parameter family of side beams support the lowest frequency BIC (black marker in Fig. 2(b)). The diamond marked geometric dimensions are used for experimental demonstration in Sec. IV.

traveling wave solutions of the form $\boldsymbol{u}_n = \tilde{\boldsymbol{u}} e^{i\kappa n}$, where κ is the non-dimensional wave-number, $\boldsymbol{u}_n = [\theta_n,\ u_n]^T$ and $\tilde{\boldsymbol{u}} = [\theta\ u]^T$. The discretized governing equations (4) for this section then reduce to an eigenvalue problem $\omega^2 \boldsymbol{M}_n(\kappa)\tilde{\boldsymbol{u}} = \boldsymbol{K}_n(\kappa)\tilde{\boldsymbol{u}}$ with

$$\boldsymbol{M}_n(\kappa) = \frac{m_b}{420}\begin{bmatrix} 2l_e^2(4 - 3\cos\kappa) + I_{y_n} & 26 l_e \sin\kappa \\ -26 i l_e \sin\kappa & 312 + 108\cos\kappa + m_n \end{bmatrix}, \quad (6a)$$

$$\boldsymbol{K}_n(\kappa) = \frac{EI}{l_e^2}\begin{bmatrix} 4l_e(2 + \cos\kappa) & -12i\sin\kappa \\ 12i\sin\kappa & 24/l_e(1 - \cos\kappa) \end{bmatrix}. \quad (6b)$$

Solving the eigenvalue problem for each κ in the interval $[0, \pi]$ gives two dispersion branches denoted by red curves in the Fig. 2(c). The first three bound mode frequencies in Fig. 2(a) lie on the lower red branch, implying that these are BICs.

IV. 3D NUMERICAL SIMULATIONS AND EXPERIMENTAL RESULTS

This section presents the verification of our predictions based on the 1D beam model using 3D elasticity theory.

The simulations are performed using a commercial finite element analysis software COMSOL. Finally, we report on the experimental observation of a BIC under dynamic excitation with a shaker.

A. Verification using $3D$ elasticity theory

We model the finite beam structure shown in Fig. 4(b) using $3D$ elasticity theory. Here, the motion at every point in a structure made of a linear elastic isotropic solid is governed by [36] $\rho\ddot{\boldsymbol{u}} - [(\lambda+\mu)\nabla(\nabla\cdot\boldsymbol{u}) + \mu\nabla^2\boldsymbol{u}] = 0$, with $\boldsymbol{u} = [u_x\ u_y\ u_z]^T$ being the vector of displacement components, μ and λ the Lamé constants of the solid. A finite element analysis is performed using COMSOL Multiphysics software and the domain is discretized using quadratic elements with tetrahedral geometry.

Let us first verify if the $1D$ beam model is accurate by comparing their corresponding dispersion surfaces for the unit cell of Fig. 1(b). Figure 2(c) displays this comparison, with the blue and red curves determined using the $3D$ and $1D$ models, respectively. The lower frequency flexural branch is quite close for the two models, which demonstrates the effectiveness of the $1D$ beam model in predicting flexural modes based BICs. In addition, the $3D$ analysis also shows a quadratic bending along the y-direction, linear longitudinal and torsional dispersion branches.

Let us now determine the final design using $3D$ finite element analysis. All cylinders attached to the main and side beams are taken to be identical to simplify fabrication. Our starting design point is indicated by the diamond marker in Fig. 3, with side beam dimensions (l_s, w_s, h_C) = (28 mm, 5.81 mm, 5.37 mm). We do a detailed $3D$ analysis and make minor changes to the design predicted using the $1D$ beam theory. There are two reasons for requiring modifications to the design predicted using the $1D$ model. First, the rigid masses are assumed to be a point mass and the space occupied due to the finite diameter d is neglected in the $1D$ model. The second reason is to simplify assembly of masses in the side beams, the side beam is made longer to 40 mm and masses are attached at a distance l_s, as shown in Fig. 4(b). This design is distinct from the $1D$ beam model, where the cylindrical mass on the side beams are attached at their ends.

We search for suitable l_s and w_s by doing a parametric sweep over these variables near the starting design point using $3D$ finite element simulations. This choice is guided by the existence of 1-parameter family of valid design solutions of Eqn. (5), see Fig. 3. The sweep search yields (l_s, w_s) = (28 mm, 8.23 mm) when the height and diameter of all the attached cylinders are set to $h = 4.6$ mm and $d = 5$ mm, respectively. Figure 5(a) displays the BIC mode shape confined to the compact region for these side beam dimensions. Note that, the frequency determined with the $3D$ model (682.5 Hz) is close to that predicted by the $1D$ model (713 Hz). To verify that the mode in Fig.5(a) is indeed a BIC, the conventional approach is to determine the transmittance into the far-field near the BIC frequencies [37]. Since we work with a finite structure, we instead determine the ratio of kinetic energies at sections inside (A) and outside (D) the compact region at the steady state. This computation is done using $3D$ finite element analysis. Figure 7 shows that the ratio $(v_D/v_A)^2$ goes to zero at the mode's frequency, thus verifying its BIC property. Our bound modes lie in the category of Fabry-Pérot BICs, where a wave is confined between two resonators [25, 26].

We demonstrate the effect of violating reflection symmetry in the proposed design. To this end, we performed $3D$ finite element analysis on a design that breaks reflection symmetry about the y axis, as shown in the fig. 9(a). We change the rigid cylinder locations on the right side beams. The mode shape localized in the compact region now has a different frequency (756 Hz) than the BIC frequency (682.5 Hz). The out-of-plane displacement of this mode is illustrated in Fig. 9(b). We observe that the region to the left of the compact region experiences a lower leakage than the right side.

We remark that a BIC can in principle be supported on asymmetric side beams, in which case, the left and right side beams will have to be designed separately. In particular, they need to satisfy the constrains for force and moment equilibrium and conditions of zero degrees of freedom, as discussed in Sec. III.

B. Experimental observation of a BIC

Finally, we report on the experimental observation of the BIC shown in Fig. 5(a) using the dimensions determined from the $3D$ analysis. The experimental setup is shown in Fig. 4(a). The structure in Fig. 4(b) is fabricated from a 0.08 inch thick Aluminum 6061 sheet using water-jet cutting. Cylindrical Neodymium magnets N35 of 5mm diameter and 4.6mm height are placed at the top and bottom in the main and side beams. These dimensions are chosen since they are commercially available. The sample is clamped at both ends and a permanent magnet shaker (LDS V203) is used to apply sinusoidal displacement at the center of the compact region. The excitation point is denoted here by A, as shown in Fig. 5(a). A force sensor (PCB 208C01) is attached to the shaker to measure the applied force. The velocity at various points along the main beam is measured using a laser Doppler vibrometer (Polytec VFX-I-110).

Let us summarize the experimental procedure. We excite the structure at different frequencies in the interval $[650, 750]$ Hz and determine the frequency response function. The excitation frequencies are indicated by markers in the response plot in Fig. 5(a). The velocity of a cylinder and the force applied by the shaker are measured by applying the excitation at a frequency for 15 seconds. To allow transients to die down, the force and velocity data are recorded in the last 6 seconds of excitation. Then

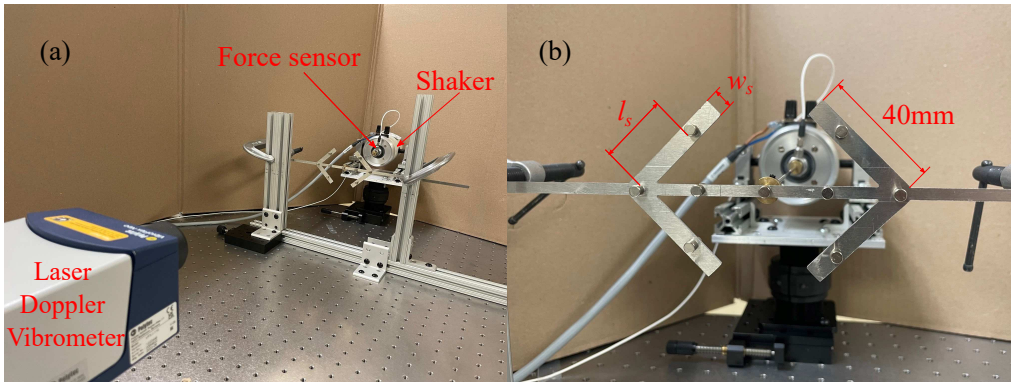

FIG. 4. (a) Experimental set-up. The beam is exited at the center of the compact region using a shaker. A force sensor is attached to the shaker. The velocity at various points along the beam is measured using a laser vibrometer. (b) Zoomed-in view, indicating the dimensions l_s and w_s in a 40 mm side beam length.

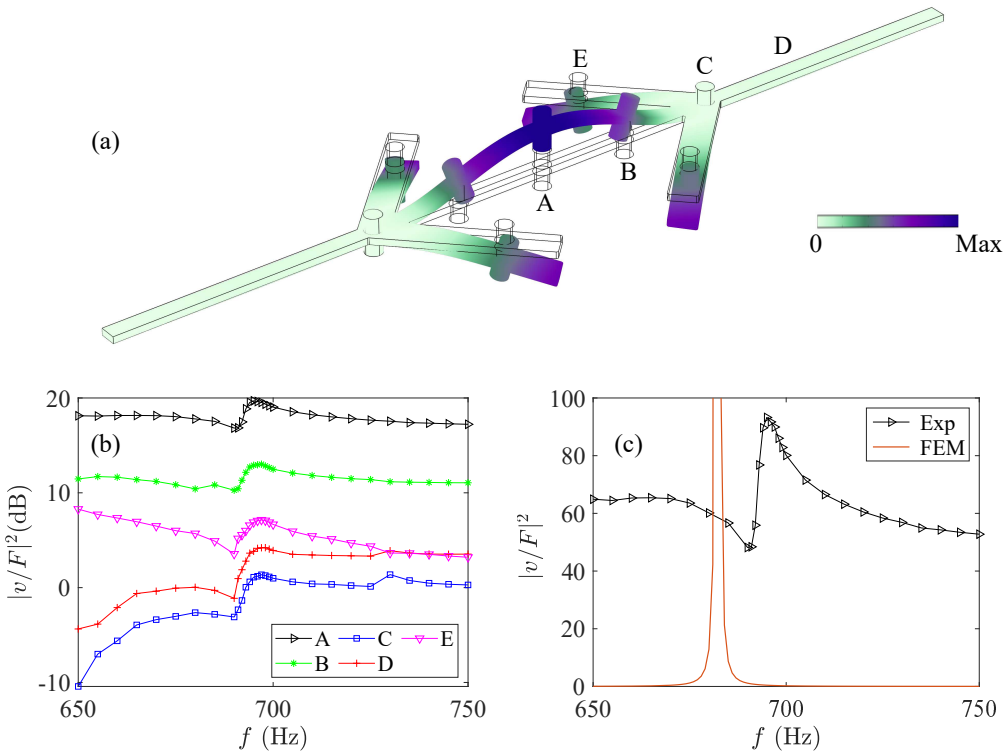

FIG. 5. (a) BIC mode shape at 682.5 Hz determined using $3D$ FEA. (b) Measured frequency response at cylinders. A resonant peak occurs at 695 Hz corresponding to the BIC. (c) Comparison of frequency response at excitation point A: lossless simulation and experiments.

the beam is kept at rest for 10 seconds before exciting it at next frequency. This process is repeated for measuring velocity of each cylinder. The maximum velocity, v and maximum force, F at a frequency are calculated by a FFT of the measured velocity and force. Then, normalized energy of every point is determined as $|v/F|^2$.

Figure 5(b) displays the measured response at cylinders on the right side of excitation point. We observe a peak in the frequency response of the excitation point A at 695 Hz. At this frequency, the response at points C and D, lying at the boundary and outside the compact region, are significantly lower (1 unit) compared to the excitation point A (about 93 units). This observation confirms the existence of a BIC in the structure at 695 Hz. We also measured the frequency response at other cylinders left of the excitation point. Note that due to reflection symmetry, the corresponding symmetric points on the left should have identical response. We quantified the difference in response at points B, C, D and the side beams with their corresponding symmetric points to the

left at the BIC frequency. Our experiments showed a 3% difference point B and at the side beams, and a 10% difference at points C and D with their corresponding symmetric points to the left.

Figure 5(c) displays a comparison between experiments and lossless simulations for the frequency response at the excitation point. The simulation has a response peak (around 1000 units) at 682.5 Hz, which is the frequency of the mode shape in Fig. 5(a). Let us remark on the various sources of error that result in deviation from a true BIC. We conducted additional simulations to identify the source of discrepancy between simulations and experiments. In particular, we conducted simulations considering material loss and perturbed geometry. Details are presented in Appendix C. The discrepancy between experiments and simulations is attributed to imperfections in manufacturing, with the fabricated beam width being around 4.8 mm instead of the designed 5mm, and precision in placing cylinders at the exact locations. Since our numerical simulation with $3D$ finite element analysis predicts high quality factors, we believe the mismatch between simulation and experiments arise due to limitations of our fabrication and assembly process. However, this is not a fundamental limitation of the proposed framework and it is one that can be addressed in principle. Indeed, with recent advances in precision machining at the micro- and nano-scales, we believe that the quality factor can approach that predicted by numerical simulations.

Finally, we note that the frequency response point C is 0.137 units in simulations, compared to 1000 for point A. Although significantly lower than the experimental value, it is not zero, in contrast to the prediction of the $1D$ beam model. To understand this discrepancy, note that the Euler Bernoulli beam theory, which is used to predict a true BIC, assumes that each cross-section is non-deformable, and undergoes translations and rigid rotations [38]. Although an excellent approximation at low frequencies, small deviations arise when full $3D$ effects are considered. The resulting displacement at C is thus a measure of the deviation of the exact $3D$ solution from the $1D$ beam theory. Notably, we do not attempt to satisfy the zero displacement condition point-wise, but instead do it in an average sense over the entire cross-section.

V. CONCLUSION

We introduce the architected structure that comprises of a main beam with periodically attached masses, and has a compact region with protruding side beams. Symmetry and equilibrium constraints are used to determine the conditions required for a BIC in this compact region. A $1D$ beam model is derived using Euler Bernoulli theory and a finite element method is used to determine bound modes in the structure. The conditions on main and side beams required to support a BIC are derived and a Newton Raphson method is used to solve the resulting nonlinear equations. For each BIC, we find a 1-parameter family of side beam designs that supports it. A dispersion analysis is conducted to confirm that their frequencies lie in passband and they are thus BICs.

We verify the predictions of BIC based on the $1D$ beam model using finite element analysis (FEA) based on $3D$ elasticity. The $1D$ model is found to be in good agreement for the low frequency flexural modes under consideration. For ease of fabrication and assembly, and to account for the mismatch with $3D$ elasticity, minor modifications to the side beam design determined using the $1D$ model are made by doing a parametric sweep over the width and length of side beams using $3D$ FEA. The designed structure is fabricated and excited over a range of frequencies around the BIC frequency. The experimental results of frequency response at the excitation point shows a resonant peak close to the frequency predicted by FEA. At the resonant frequency, the fraction of energy leaking to surrounding reduced to minimum, which demonstrates the existence of a BIC in the compact region. The experimental results are compared with FEA results and the possible reasons for discrepancies, along with causes of deviation from a true BIC are discussed.

Let us remark on some future possible extensions of our work. These concepts translate across length scales and material properties, and may find applications at the micro and nano-scales. At those scales, the limitations associated with material damping may be significantly reduced. The idea of cancelling forces and moments by exploiting symmetry may be extended to realize bound modes and BICs in plates, shells and $3D$ architected solids. Our framework is relevant in physical domains beyond the elastic structures considered here, for instance in the photonic crystal waveguides with off-channel defects, in which BICs were predicted earlier [26].

ACKNOWLEDGMENTS

This work was supported by the U.S. National Science Foundation under Award No. 2027455

Appendix A: Finite element shape functions and matrices

Let us discuss an approximation we use to determine the effective bending stiffness of the beam segment between sections 1 and 2 in Fig. 6. Its contribution comes from three segments: the two segments of length $d/2$ at the two ends having rigid masses, and the beam segment with length $l_e = l - d$ between them. These three segments may be viewed as springs in series and their effective stiffness is lower than the stiffness of these segments. The segment having rigid masses (length $d/2$) has significantly higher bending stiffness and its contribution to the effective bending stiffness is neglected. Only the

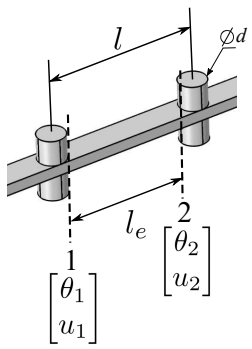

FIG. 6. Schematic of a beam finite element with degrees of freedom $[\theta_1,\ u_1]^T$ and $[\theta_2,\ u_2]^T$ at sections 1 and 2, respectively.

beam segment l_e in Fig. 6 is used to determine the effective bending stiffness. Under this approximation, the rigid masses may be represented as point masses with a beam segment of length l_e between them.

Figure 6 displays a schematic of a beam finite element. The discrete degrees of freedom are the displacements and rotations at the location of rigid masses, labeled $[\theta_1,\ u_1]^T$ and $[\theta_2,\ u_2]^T$ in this figure. Let us denote the location of point 1 and 2 by x_1 and x_2, respectively. In this element, we seek a solution of the form

$$u(x) = N_1(\xi)\theta_1 + N_2(\xi)u_1 + N_3(\xi)\theta_2 + N_4(\xi)u_2, \quad \text{(A1)}$$

where ξ is a local coordinate in the element given by $(x - x_1)/l_e$ and taking values in $[0, 1]$. $N_i(\xi)$ are Hermite polynomial shape functions [39] and explicit expressions for the shape functions are

$$N_1 = l_e\xi(\xi - 1)^2 \quad \text{(A2a)}$$
$$N_2 = 1 - 3\xi^2 + 2\xi^3 \quad \text{(A2b)}$$
$$N_3 = l_e\xi^2(\xi - 1) \quad \text{(A2c)}$$
$$N_4 = \xi^2(3 - 2\xi) \quad \text{(A2d)}$$

Here, Eqn. (A1) may be written compactly as $u(x) = \boldsymbol{N}\boldsymbol{u}^T$, with $\boldsymbol{N}$ and $\boldsymbol{u}$ being vectors having components N_i and u_i, respectively.

Let us derive the contribution of the above beam segment to the governing equation. We substitute Eqn. (A1) into Eqn. (3) and separate the terms with and without ω^2 into mass matrix, $\boldsymbol{M}_{el}$ and stiffness matrix, $\boldsymbol{K}_{el}$ respectively for an element. The various terms in Eqn. (3) then have the form $\delta\boldsymbol{u}^T\boldsymbol{K}_{el}\boldsymbol{u}$ or $\omega^2\delta\boldsymbol{u}^T\boldsymbol{M}_{el}\boldsymbol{u}$, where

$$\boldsymbol{K}_{el} = \int_{x_1}^{x_2} \frac{d^2\boldsymbol{N}^T}{dx^2} EI \frac{d^2\boldsymbol{N}}{dx^2} dx, \quad \text{(A3)}$$

$$\boldsymbol{M}_{el} = \int_{x_1}^{x_2} \rho A \boldsymbol{N}^T\boldsymbol{N} dx + \sum_{i=1}^{2} m_i \boldsymbol{N}^T(\xi_i)\boldsymbol{N}(\xi_i) + \sum_{i=1}^{2} I_i \frac{d\boldsymbol{N}^T(\xi_i)}{dx}\frac{d\boldsymbol{N}(\xi_i)}{dx}. \quad \text{(A4)}$$

Here, x_1 and x_2 are respectively locations for section 1 and 2 in Fig. 6. The m_i and I_i represent mass and mass moment of inertia of ith rigid mass, respectively. Explicit expressions for these matrices are

$$\boldsymbol{M}_{el} = \frac{m_b}{420}\begin{bmatrix} 4l_e^2 + I_1 & 22l_e & -3l_e^2 & 13l_e \\ 22l_e & 156 + m_1 & -13l_e & 54 \\ -3l_e^2 & -13l_e & 4l_e^2 + I_2 & -22l_e \\ 13l_e & 54 & -22l_e & 156 + m_2 \end{bmatrix} \quad \text{(A5a)}$$

$$\boldsymbol{K}_{el} = \frac{EI}{l_e^3}\begin{bmatrix} 4l_e^2 & 6l_e & 2l_e^2 & -6l_e \\ 6l_e & 12 & 6l_e & -12 \\ 2l_e^2 & 6l_e & 4l_e^2 & -6l_e \\ -6l_e & -12 & -6l_e & 12 \end{bmatrix}. \quad \text{(A5b)}$$

Here, $m_b = \rho A l_e$ is the mass of the beam in the element. Assembling $\boldsymbol{M}_{el}$ and $\boldsymbol{K}_{el}$ for every beam segment in the structure gives its mass $\boldsymbol{M}$ and stiffness $\boldsymbol{K}$ matrix. The governing equations result in an eigenvalue problem $\omega^2\boldsymbol{M}\boldsymbol{u} = \boldsymbol{K}\boldsymbol{u}$. Here, $\boldsymbol{u}$ is a vector with components having the displacements and rotations at the rigid mass locations.

Appendix B: Transmittance to far field

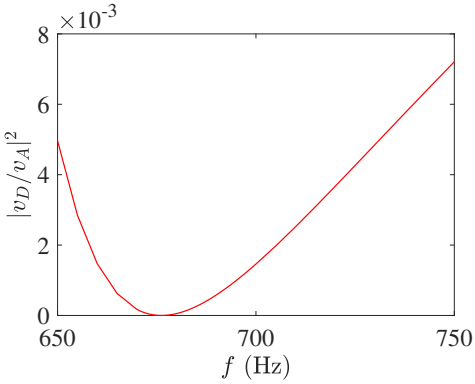

FIG. 7. Ratio of kinetic energies at sections outside and inside the compact region goes to zero at the BIC frequency. Steady state results from $3D$ finite element analysis.

Appendix C: Simulations with material loss and imperfect geometry

To identify the source of discrepancy between simulations and experiments, we conducted simulations for two other cases that consider material loss and deviation from exact geometry:

- Considering material loss. We consider the loss factor of 0.01 for both aluminum and magnet.
- Introducing perturbation in $3D$ model. We change the location of every cylinder pairs from the location in theoretical design by a random value in the interval of $[-4\%\ 4\%]$ of the unit cell length along corresponding beam axis. This perturbation aims to consider the error caused due to attaching the magnets by hand in the structure.

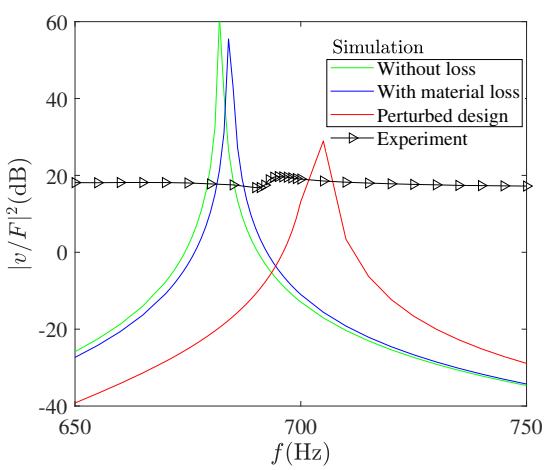

FIG. 8. (a) Schematic of a structure violating reflection symmetry about y-axis. Attached cylinders are marked by black circles. (b) Out-of-plane displacement along main beam at 756 Hz, which is the closest to the observed BIC frequency. The BIC in the compact region between A and B cannot exist due to violating symmetry about the x axis.

The frequency response for all cases, including the simulation with lossless perfect geometry, is presented in Fig. 8. Also shown is the experimentally measured response. We observe that the effect of material loss (blue curve) is negligible on the quality factor. In contrast, the change in geometry due to deviation in magnet location (red curve) results in a significant reduction in quality factor, as well as a shift in frequency. A similar frequency shift is also observed in the experiment. Based on these results, we conclude that imperfections in manufacturing and assembly have a more significant effect on the quality factor compared to material loss in the considered frequency regimes.

Appendix D: Effect on BIC for breaking symmetry along the x axis

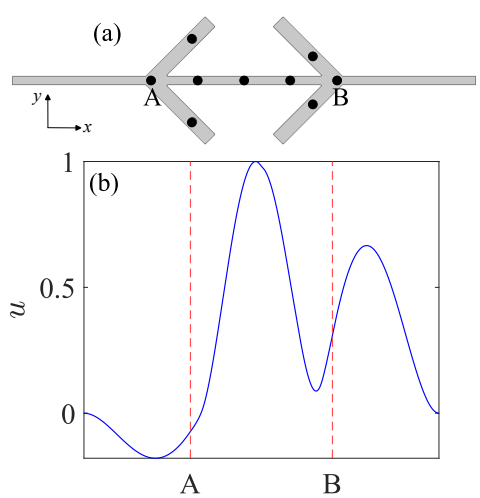

FIG. 9. (a) Schematic of a structure violating reflection symmetry about y-axis. Attached cylinders are marked by black circles. (b) Out-of-plane displacement along main beam at 756 Hz, which is the closest to the observed BIC frequency. The BIC in the compact region between A and B cannot exist due to violating symmetry about the x axis.

Appendix E: 1-parameter family of designs for other BICs

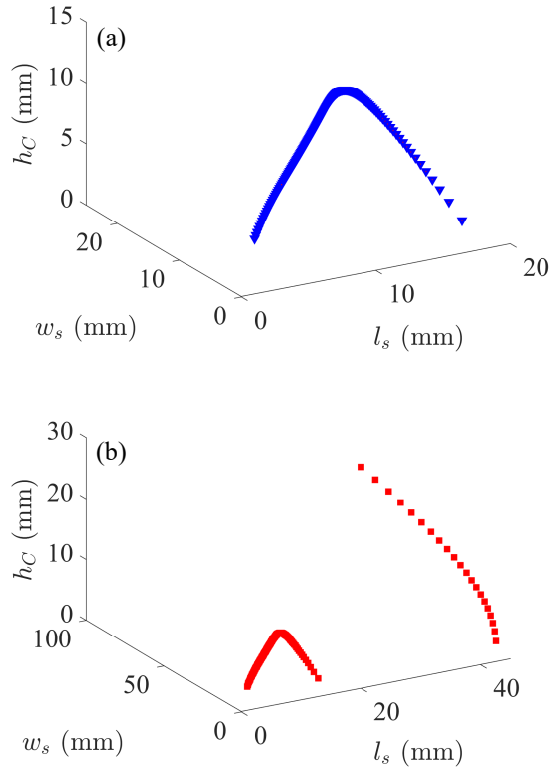

FIG. 10. 1-parameter family of side beam design that support the BICs marked by blue (a) and red (b) markers in Fig. 2(b), respectively. The curve in (b) is continuous. It looks discontinuous as the design variables take negative values (not shown).

[1] C. W. Hsu, B. Zhen, A. D. Stone, J. D. Joannopoulos, and M. Soljačić, Bound states in the continuum, Nature Reviews Materials **1**, 1 (2016).

[2] S.-H. Jo, H. Yoon, Y. C. Shin, and B. D. Youn, A graded phononic crystal with decoupled double defects for broadband energy localization, International Journal of Mechanical Sciences **183**, 105833 (2020).

[3] A. Khelif, A. Choujaa, B. Djafari-Rouhani, M. Wilm, S. Ballandras, and V. Laude, Trapping and guiding of acoustic waves by defect modes in a full-band-gap ultrasonic crystal, physical Review B **68**, 214301 (2003).

[4] R. Marchal, O. Boyko, B. Bonello, J. Zhao, L. Belliard, M. Oudich, Y. Pennec, and B. Djafari-Rouhani, Dynamics of confined cavity modes in a phononic crystal slab investigated by in situ time-resolved experiments, Physical Review B **86**, 224302 (2012).

[5] J. v. Neumann and E. P. Wigner, Über merkwürdige diskrete eigenwerte, in *Phys.Z.*, Vol. 30 (1929) p. 465.

[6] L. Fonda, Bound states embedded in the continuum and the formal theory of scattering, Annals of Physics **22**, 123 (1963).

[7] F. H. Stillinger and D. R. Herrick, Bound states in the continuum, Phys. Rev. A **11**, 446 (1975).

[8] R. Parker, Resonance effects in wake shedding from parallel plates: some experimental observations, Journal of Sound and Vibration **4**, 62 (1966).

[9] K. Koshelev, A. Bogdanov, and Y. Kivshar, Meta-optics and bound states in the continuum, Science Bulletin **64**, 836 (2019), sPECIAL TOPIC: Electromagnetic Metasurfaces: from Concept to Applications.

[10] M. Imada, S. Noda, A. Chutinan, T. Tokuda, M. Murata, and G. Sasaki, Coherent two-dimensional lasing action in surface-emitting laser with triangular-lattice photonic

crystal structure, Applied physics letters **75**, 316 (1999).
[11] K. Hirose, Y. Liang, Y. Kurosaka, A. Watanabe, T. Sugiyama, and S. Noda, Watt-class high-power, high-beam-quality photonic-crystal lasers, Nature photonics **8**, 406 (2014).
[12] A. Kodigala, T. Lepetit, Q. Gu, B. Bahari, Y. Fainman, and B. Kanté, Lasing action from photonic bound states in continuum, Nature **541**, 196 (2017).
[13] S. Romano, G. Zito, S. N. L. Yépez, S. Cabrini, E. Penzo, G. Coppola, I. Rendina, and V. Mocellaark, Tuning the exponential sensitivity of a bound-state-in-continuum optical sensor, Opt. Express **27**, 18776 (2019).
[14] L. L. Doskolovich, E. A. Bezus, and D. A. Bykov, Integrated flat-top reflection filters operating near bound states in the continuum, Photon. Res. **7**, 1314 (2019).
[15] J. M. Foley, S. M. Young, and J. D. Phillips, Symmetry-protected mode coupling near normal incidence for narrow-band transmission filtering in a dielectric grating, Physical Review B **89**, 165111 (2014).
[16] O. Kawachi, S. Mineyoshi, G. Endoh, M. Ueda, O. Ikata, E. Hashimoto, and M. Yamaguchi, Optimal cut for leaky saw on litao/sub 3/for high performance resonators and filters, IEEE transactions on ultrasonics, ferroelectrics, and frequency control **48**, 1442 (2001).
[17] N. F. Naumenko and B. P. Abbott, Surface acoustic wave devices using optimized cuts of a piezoelectric substrate (2003), uS Patent 6,556,104.
[18] L. Cao, Y. Zhu, S. Wan, Y. Zeng, Y. Li, and B. Assouar, Perfect absorption of flexural waves induced by bound state in the continuum, Extreme Mechanics Letters **47**, 101364 (2021).
[19] F. Benabid, J. C. Knight, G. Antonopoulos, and P. S. J. Russell, Stimulated raman scattering in hydrogen-filled hollow-core photonic crystal fiber, Science **298**, 399 (2002).
[20] F. Couny, F. Benabid, P. Roberts, P. Light, and M. Raymer, Generation and photonic guidance of multi-octave optical-frequency combs, Science **318**, 1118 (2007).
[21] A. Rahman and R. K. Pal, Bound modes in the continuum based phononic waveguides, Journal of Applied Physics **132**, 115109 (2022).
[22] C. W. Hsu, B. Zhen, J. Lee, S.-L. Chua, S. G. Johnson, J. D. Joannopoulos, and M. Soljačić, Observation of trapped light within the radiation continuum, Nature **499**, 188 (2013).
[23] Z. Sadrieva, M. Belyakov, M. Balezin, P. Kapitanova, E. Nenasheva, A. Sadreev, and A. Bogdanov, Experimental observation of a symmetry-protected bound state in the continuum in a chain of dielectric disks, Physical Review A **99**, 053804 (2019).
[24] Y. Plotnik, O. Peleg, F. Dreisow, M. Heinrich, S. Nolte, A. Szameit, and M. Segev, Experimental observation of optical bound states in the continuum, Physical review letters **107**, 183901 (2011).
[25] D. C. Marinica, A. G. Borisov, and S. V. Shabanov, Bound states in the continuum in photonics, Phys. Rev. Lett. **100**, 183902 (2008).
[26] E. N. Bulgakov and A. F. Sadreev, Bound states in the continuum in photonic waveguides inspired by defects, Physical Review B **78**, 075105 (2008).
[27] A. Taghizadeh and I.-S. Chung, Quasi bound states in the continuum with few unit cells of photonic crystal slab, Applied Physics Letters **111**, 031114 (2017).
[28] D. R. Abujetas, Á. Barreda, F. Moreno, A. Litman, J.-M. Geffrin, and J. A. Sánchez-Gil, High-q transparency band in all-dielectric metasurfaces induced by a quasi bound state in the continuum, Laser & Photonics Reviews **15**, 2000263 (2021).
[29] O. Haq and S. Shabanov, Bound states in the continuum in elasticity, Wave Motion **103**, 102718 (2021).
[30] L. Cao, Y. Zhu, Y. Xu, S.-W. Fan, Z. Yang, and B. Assouar, Elastic bound state in the continuum with perfect mode conversion, Journal of the Mechanics and Physics of Solids **154**, 104502 (2021).
[31] H. Fan, H. Gao, S. An, Z. Gu, Y. Chen, S. Huang, S. Liang, J. Zhu, T. Liu, and Z. Su, Observation of non-hermiticity-induced topological edge states in the continuum in a trimerized elastic lattice, Physical Review B **106**, L180302 (2022).
[32] Y. Yu, X. Xi, and X. Sun, Observation of mechanical bound states in the continuum in an optomechanical microresonator, Light: Science & Applications **11**, 328 (2022).
[33] H. Tong, S. Liu, M. Zhao, and K. Fang, Observation of phonon trapping in the continuum with topological charges, Nature communications **11**, 1 (2020).
[34] D. Lee, J. Park, S. Kim, J. Mun, J. Kim, X. Piao, N. Park, and J. Rho, Elastic bound states in the continuum by acoustoelastic interaction, Extreme Mechanics Letters , 101965 (2023).
[35] M. S. Dresselhaus, G. Dresselhaus, and A. Jorio, *Group theory: application to the physics of condensed matter* (Springer Science & Business Media, 2007).
[36] J. Achenbach, *Wave propagation in elastic solids* (Elsevier, 2012).
[37] A. F. Sadreev, Interference traps waves in an open system: bound states in the continuum, Reports on Progress in Physics **84**, 055901 (2021).
[38] J. M. Gere and S. Timoshenko, Mechanics of materials. ed, Boston, MA: PWS (1997).
[39] R. D. Cook, D. S. Malkus, M. E. Plesha, and R. J. Witt, *Concepts and Applications of Finite Element Analysis, 4th Edition*, 4th ed. (Wiley, 2001).